Gravity Balancing Flexure Spring Mechanisms for Shoulder Support in Assistive Orthoses

Martin Tschiersky, Edsko E. G. Hekman, *Member, IEEE*, Just L. Herder, *Member, IEEE*, and Dannis M. Brouwer

***Abstract*—Passive shoulder supports show large potential for a wide range of applications, such as assisting activities of daily living and supporting work-related tasks. The rigid-link architecture used in currently available devices, however, may pose an obstacle to finding designs that offer low protrusion and close-to-body alignment. This study explores the use of mechanisms that employ a flexible element which connects the supported arm to an attachment at the back and acts as energy storage, transmission and part of the load bearing structure. Based on the synthesis method explained in this paper, a large scope investigation into possible flexure-based mechanism topologies is conducted. Thereby, many potential designs are discovered, which are presented, categorized and compared. Two promising designs are developed into prototypes, and are built and tested on a dedicated test bench. These two mechanisms reduce the necessary moment to lift the arm by more than 80 % throughout 85 % of the range of motion, while staying within 18 cm and 10 cm distance from the body, respectively. The study indicates that, due to its lower protrusion and interface loads, a design with a tapered flexure connecting the upper arm via a hinge to a spring-loaded slider at the back offers the most promising solution.**

***Index Terms*—Gravity balancing, wearable device, assistive orthosis, shoulder support, flexure spring.**

I. Introduction

UPPER-LIMB wearable assistive devices are used to facilitate functional arm movements. By providing supporting forces and moments to the wearer they reduce the amount of muscle exertion necessary to perform manual tasks. While potentially beneficial for a wide range of use cases, they are currently mostly used and investigated in two main areas. The first pertains to people suffering from deficient motor function who can use such devices to restore their ability to perform activities of daily living (ADLs), and thus reduce their reliance on external help [1], [2]; The second concerns workers who are exposed to physically demanding tasks, and who may use them to mitigate their risk of work-related musculoskeletal disorders (MSDs) [3].

Assistive devices for the upper limb can be broadly characterized as either end-effectors or orthoses. The latter can be subdivided into rigid exoskeletons and soft exosuits. Within each category further distinctions can be made based upon the applied actuation scheme [1], [2], [4], [5], [6], [7]. Active exoskeletons and, more recently, exosuits are being extensively investigated in academic research. However, commercially available devices for assisting ADLs are predominantly passive end-effectors [1], while work-assist devices that support the upper limb are exclusively passive exoskeletons [3].

Considering passive orthoses that provide dynamic shoulder support, five potentially fully wearable devices designated for assisting ADLs exist to the authors' knowledge. The A-Gear [8], Panto-Arm Exo [9] and SpringWear [10] are academic research prototypes, while the EksoUE [11] and Wilmington Robotic Exoskeleton (WREX) [12], [13] are commercially available devices. On the other hand, in recent years several companies have entered the market with wearable work-assist exoskeletons. Examples are: the Airframe [14], [15], EksoVest and EVO [11], [16], MATE [17], [18], PAEXO [19], [20], ShoulderX [21], [22] and SkelEx [23], [24].

All the above mentioned are passive devices that work by applying forces and moments to the wearer's upper limb which counter the gravity loads acting upon it. Thus, the amount of force the user has to exert in order to lift the arms is reduced. To this end, these exoskeletons employ rigid-link mechanisms that contain energy-storing elements like tension and compression springs [14], [17], [21], gas springs [9], [11], rubber bands [8], [10], [12], [19] and leaf spring flexures [23] in combination with transmission elements like rigid linkages [8], [9], [10], [12], [19], [23], cable-pulley configurations [14], [21], gears [17] and cams [11] which together create the desired mechanical behavior. These types of mechanisms, however, imply an exoskeleton design in which a rigid frame and rigid links are used to interface with the wearer's body. Such being the case, additional links, joints and sliders are added to make the largely rigid structure adjustable and comply with the shoulder kinematics, increasing the complexity and number of parts necessary. Furthermore, to avoid potentially harmful collision moving parts are required to maintain a safe distance to the body, often leading to significant protrusion.

The research presented in this paper attempts to address these issues. In the presented design approach a flexible element resembling a curved flexure with variable thickness is connected between the user's back and upper arm. Like in the SkelEx device, this flexure acts as both the energy-storing element and as part of the frame. However in contrast, the flexure is designed to be more compliant and exhibit large

Manuscript received November 18, 2020; revised August 21, 2021; accepted February 11, 2022. Date of publication February 28, 2022; date of current version May 18, 2022. This article was recommended for publication by Associate Editor Q. Wang and Editor P. Dario upon evaluation of the reviewers' comments. This project has received funding from the European Union's Horizon 2020 research and innovation programme under grant agreement No. 688857 (SoftPro). *(Corresponding author: Martin Tschiersky.)*

Martin Tschiersky and Dannis M. Brouwer are with the Chair of Precision Engineering, University of Twente, 7500 AE Enschede, The Netherlands (e-mail: m.tschiersky@utwente.nl).

Edsko E. G. Hekman is with the Department of Biomechanical Engineering, University of Twente, 7500 AE Enschede, The Netherlands.

Just L. Herder is with the Department of Precision and Microsystems Engineering, Delft University of Technology, 2628 CD Delft, The Netherlands.

This article has supplementary downloadable material available at https://doi.org/10.1109/TMRB.2022.3155293, provided by the authors.

Digital Object Identifier 10.1109/TMRB.2022.3155293

deformations. Furthermore, no additional links between the arm and the back are used to prescribe its deformation and to create the gravity-balancing properties. Instead, by utilizing the natural shoulder kinematics, the gravity-balancing behavior emerges from the shape of the flexure in combination with the kinematic constraints prescribed at each end. Thus, the flexure integrates functions of energy storage, transmission and the load-bearing structure. This approach is used to obtain devices that are structurally more compliant than current exoskeletons, while preserving comparable external load bearing capabilities. Utilizing the gain in flexibility, the goal is to bring the device closer to the wearer's body, as due to the yielding nature of the flexure it is hypothesized that the wearer would not incur any harm in the event of a collision. Furthermore, the flexure may offer the necessary compliance to compensate for small alignment errors and to allow limited motion in the unsupported directions. Together with the above described function integration this may reduce the overall complexity and lead to a smaller part count.

To find appropriate designs, a computational model is created which encompasses the flexible element and the wearer, to simulate the mechanical behavior of the entire system and to determine the distance between the two. Using this model, flexure shapes are optimized for various support conditions at each end, to find flexure spring mechanisms that offer both adequate gravity-balancing support and close-to-body alignment. The approach is based on our previous work concerning gravity-balancing flexure springs for an assistive elbow orthosis [25] and similar work on gravity-balancing flexure mechanisms within [26], [27] and without [28], [29], [30] the context of assistive devices. However, the method is expanded by introducing a new use case, multiple design objectives and more complex spatial constraints, in which collision with the body is to be avoided while remaining in close proximity to it. Furthermore, an extensive investigation is conducted to examine the effects of using different kinematic support conditions at each end of the flexure, representing sliders, hinges and combinations thereof with zero, non-zero finite or infinite stiffness.

Following this introduction the *Synthesis* section describes the applied methods by which gravity-balancing flexure spring mechanisms for several different kinematic support conditions are obtained. From these, two support conditions are selected for further investigation, from which two prototype designs are derived. The subsequent *Experiment* section deals with the physical validation of these prototypes on a dedicated test bench. The outcomes of both the synthesis and experiment are presented in the *Results* section and reflected upon in the *Discussion* section. Lastly, the key insights are provided in the *Conclusions* section.

II. Synthesis

A. Model Topology

For the design of the flexure mechanisms, the flexible element with its end supports, as well as the torso and right arm of the wearer are considered. The schematic model topology is shown in Figure 1. Mechanically, the shoulder joint is reduced to a pair of revolute joints which are connected to each other and coincide with the position of the glenohumeral joint. The joints are oriented perpendicular to each other and their motion corresponds to the upper arm elevation θ and horizontal flexion/extension γ, respectively. Their position in space is fixed with respect to ground. In order to simplify the model

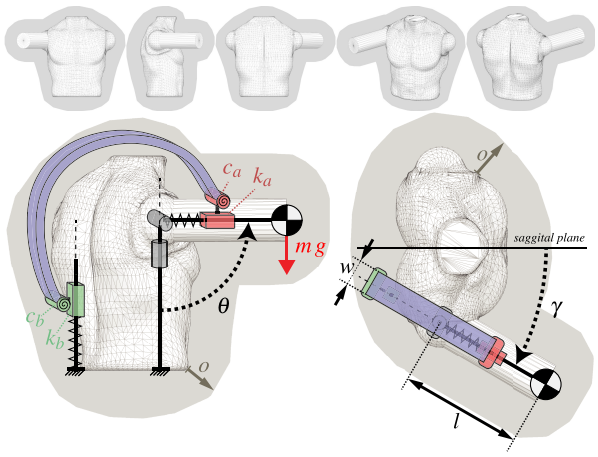

Fig. 1. Model topology. The triangulated meshes for the torso and right upper arm are shown in white, the offset mesh volume is indicated in gray. The top figures show the meshes from several perspectives. The bottom left figure is a view perpendicular to the arm elevation plane. The bottom right figure is a view from the top. Rigid links are shown as black bold lines. Their axes are indicated by dashed lines. The prismatic and revolute joints are drawn in gray for the shoulder, red for the arm interface and green for the back interface. The flexible element, i.e., the flexure, is shown in blue.

for both optimization and experimental validation, scapulothoracic motion as well as endo/exorotation are not considered. The arm itself is treated as a rigid link with a mass m located at the center of gravity and is connected to the pair of revolute joints at its proximal end. The position of the mass is fixed as elbow and hand motion are not considered.

The flexible element is treated as a prismatic beam with a rectangular cross-section and a varying thickness along its length. It is connected to a point at the back of the wearer at one end, travels above the top of the right shoulder, and connects to the upper arm section of the arm link at the other end. At each interface point the flexure is connected via a slider/hinge combination. The slider at the back allows motion along the vertical axis and the slider on the arm motion along the arm axis. The orientation of the hinges is perpendicular to the arm elevation plane. By setting the stiffnesses of these kinematic elements, each connection can be modeled as either a clamp, slider, hinge or a combination of both slider and hinge. In addition, when using non-zero finite stiffness values, each element can also act as a spring with a translational stiffness k or rotational stiffness c, respectively.

The volumes of the torso and right upper arm are represented by triangulated meshes. The position and orientation of the torso mesh is fixed, while the upper arm mesh orientation follows the arm link. For each mesh a corresponding offset mesh with a uniform offset o prescribes the space in which the flexible element is allowed to operate.

B. Design Objectives

The primary goal of this study is to find the ideal shape and thickness distribution of the flexible element, and the ideal joint stiffness values for each prescribed kinematic support condition, such that the resulting mechanism balances the mass m on the arm link, while not colliding with, but staying within close proximity to the wearer. This should be achieved while featuring a small flexure width to reduce the overall size, protrusion and out-of-plane stiffness. Furthermore, to allow for a design in which the flexible element can be directly connected

to the arm, parasitic forces and moments that do not contribute to the gravity-balancing behavior should be minimal. To this end, four metrics are used to assess the quality of a design.

Gravity balancing quality is the primary objective. It is defined as the ability of the flexure mechanism to counteract the effect of gravity on a mass m, such that the moment M at the shoulder elevation joint is zero for any elevation angle θ in the range from 0 to π. For the given model, the moment caused by gravity can be expressed as:

$$M_g = a_g \sin(\theta) \qquad a_g = -mgl \tag{1}$$

where a is the moment amplitude, g the gravitational acceleration and l the distance between the center of gravity and the shoulder joint. Consequently, the moment M_f exerted by the flexure mechanism has to be the inverse. However, M_g and M_f are normalized by their respective maximum amplitude to obtain the relation for the ideal case:

$$\frac{M_f}{a_f} - \sin(\theta) = 0 \qquad a_f = \max\left(|M_f|\right) \tag{2}$$

The gravity balancing quality can now be expressed by the cumulative error in this equation for the considered range of motion. Since the elevation angle in both simulation and experiment is discretized, the normalized mean absolute error (NMAE) is chosen for this purpose:

$$\boldsymbol{\delta} = \sum_{i=0}^{n} \frac{\left|\frac{M_{f,i}}{a_{f,i}} - \sin(\theta_i)\right|}{n} \tag{3}$$

where i is a data point and n the total number of data points.

The second metric is the ratio between the maximum moment amplitude and the flexure width w. It serves as an indicator for the relative strength of a design. It is defined as:

$$\boldsymbol{\epsilon} = \frac{a_f}{w}. \tag{4}$$

The third metric is the maximum protrusion of the flexible element from the body. It is measured as the maximum distance between the left or right edge of the flexure's neutral plane, i.e., mid-plane, to the respective closest position on the combined torso and arm mesh.

Finally, the fourth metric is the maximum relative shear force, defined as the ratio between the maximum shear force at the arm interface and the maximum moment amplitude. The shear force is the force component at the arm interface parallel to the arm axis. It is defined positive when pointing in distal direction, and negative when pointing in proximal direction.

C. Application Requirements

The device is intended to assist in the lifting of the arms when no additional payload is considered. This type of support is rather task independent and would potentially benefit both prior mentioned use case scenarios of assisting ADLs and physically demanding work-related tasks. The device shall work for the entire range of motion of the shoulder from the relaxed arm position at $\theta = 0$ to the raised position at $\theta = \pi$.

In order to provide adequate gravity compensation, both the balancing quality and the balancing quantity have to be sufficient. Based on the experience from previous work [25], it is determined that a NMAE ≤ 0.05 would constitute a good balancing behavior. Regarding the quantity, it is calculated that based on the mean body segment data of female and male subjects [31] a moment amplitude of 9.16 Nm would be necessary to fully compensate for the gravity loads acting upon the arm. Based on this number a target moment amplitude of 10 Nm is chosen, offering a margin for customization.

The protrusion of the device from the body should be minimal. A study on passive assistive orthoses found that devices should stay within 30 mm from the body, and to be wearable underneath clothing even below 20 mm [2]. However, considering existing passive assistive shoulder supports, these figures seem overly ambitious. Therefore, no hard requirement is derived. Instead, this design aspect is treated as a main point of investigation.

It is known from literature that contact pressure and shear applied to the skin should be minimal in order to comfortably use a device for extended periods of time [32]. However, no practical threshold values that pertain to the presented use case could be found in literature. Therefore, this aspect is also left open for investigation.

D. Additional Specifications

This study is limited to planar mechanism designs. This is done in order to reduce the number of design parameters for the optimization. In addition, to reduce simulation effort the arm elevation is only investigated in one plane. To this end, an elevation plane with a horizontal extension angle of $\gamma = \frac{\pi}{6}$ towards the saggittal plane is chosen. Regarding the protrusion criterion, heightened attention is placed on arm elevations between $\theta = 0$ and $\theta = \frac{\pi}{2}$, since a low protrusion is deemed more critical for ADLs of which most only require this range of motion [33]. A model of a 183 cm tall male subject is used for reference to determine collision with and protrusion from the torso. The upper arm is assumed to be a cylinder with 10 cm diameter and 30 cm length.

E. Computational Model

To analyze the mechanisms in this study the flexible multibody dynamics software package SPACAR [34] is used. SPACAR is based on non-linear finite element theory for multi-degree-of-freedom mechanisms and features an application programming interface which allows for easy integration with the MATLAB environment. The mechanisms are modeled using finite two-node elements, specifically hinges and beams. The beam elements feature geometric nonlinear behavior and flexibility which is formulated in six discrete deformation modes.

At the shoulder a hinge corresponding to the arm elevation is fixed to the ground at one end and connected to the arm link at the other. Its position marks the origin of the Cartesian coordinate system. The arm link is modeled as a beam with one released deformation mode that corresponds to its elongation. As it can only permit motion along its axis and otherwise acts rigid, it can be used to model a slider with a linear stiffness k_a. A small perpendicular rigid beam extends from the arm link, i.e., the arm axis, to a position 2 cm above the surface of the arm cylinder. At this position, which serves as the interface point to the flexure, a hinge with a rotational stiffness c_a is placed to connect arm and flexure. At the back a similar construction is used to model the vertical slider with linear stiffness k_b and the back hinge with rotational stiffness c_b, though in this case no extension beam is used.

Setting the stiffnesses to infinite, zero or non-zero finite values enables the modeling of clamps, hinges, sliders and slider/hinge combinations at each interface point, with and without springs acting in parallel to the joints. A point mass of 0.2 kg is assigned to the back interface to account for the weight of the mechanical components.

The flexure which connects the hinge at the back to that on the arm is modeled as a chain of multiple beam elements that allow initial pre-curvature [35] and are fully released, thus exhibit full flexible behavior. By definition the chain starts at the back and ends at a point above the shoulder joint. The initial position of the back slider and hinge are set according to the start position of the beam. Similarly, the initial length of the arm link and the initial elevation angle of the shoulder hinge are set such that the arm interface point coincides with the end of the flexure. As a consequence and since no pre-tension is applied, the elevation angle that corresponds to the unstressed position of the mechanism depends on the flexure design.

The mesh of the torso is derived from a CAD model of a full human body. The head, arms and lower extremities are removed and spherical volumes are placed at the positions of the glenohumeral joints. The position of the right glenohumeral joint is made to coincide with the shoulder hinge. The torso is rotated about the origin to set the relative angle $\gamma = \frac{\pi}{6}$ between the plane of the mechanism and the torso's sagittal plane. The cylinder mesh representing the upper arm is translationally fixed to the origin at its proximal end and is aligned with the upper arm link. The offset meshes for the torso and arm are generated from the original collision detection meshes using a voxel-based approach, and placed and oriented in the same way.

F. Simulation

To analyze a mechanism design, a kinetostatic analysis is performed. The shoulder hinge which is controlling the arm elevation is first moved from its arbitrary initial position to the fully raised position at $\theta = \pi$. Then the shoulder hinge is rotated from $\theta = \pi$ to $\theta = 0$ in a number of predefined load steps n. In addition, gravity is imposed to account for the point mass as well as the mass of the flexure. For each load step the moment at the shoulder hinge, as well as the forces and moments at the interface points are evaluated. Furthermore, based on the node positions and orientations as well as the width of each flexible beam element constituting the flexure, contact nodes are projected onto the vertices of each beam's virtual neutral plane. These contact nodes are used to determine whether a beam lies within the torso mesh, arm mesh or their respective offset meshes. Based on that information, the protrusion distance from, or the penetration depth into the torso and arm mesh is measured for each contact node throughout the entire range of motion.

G. Parametrization

In order to optimize a mechanism its components have to be parameterized. The neutral axis of the flexure, and thus the node positions and orientations for each beam element, is obtained by constructing a Frenet ribbon with minimum torsion [36] from a natural cubic spline curve which interpolates a number of control points. The position of the first control point is given explicitly by its coordinates, while all other points are obtained through a linkage chain formulation similar to the one used in [25]. To this end, the first two parameters of the parameter set are the horizontal position s_x and the vertical position s_z of the starting point at the back. These are followed by a number of link lengths l and angles φ corresponding to the number of links in the linkage chain and consequently to the number of additional control points. An illustration of such a linkage chain can be found in [25], though for this study instead of relative angles between links, absolute angles towards the ground are used. The thickness of each beam element is obtained by linear interpolation of the thickness parameters t over the beam nodes. The mean value of the thickness values at the two nodes of each beam element yields its thickness in the computational model. An illustration of this can also be found in [25], though instead of multipliers, absolute thickness values are used. Lastly, depending on the investigated support conditions for the flexure, the stiffness values of the slider and hinge elements are appended, yielding a parameter set in the form:

$$\mathbf{x} = \big[\quad [s_x, s_z],\ [l_1, \ldots, l_n],\ [\varphi_1, \ldots, \varphi_n], \\ [t_1, \ldots, t_n],\ [k_a, c_a, k_b, c_b] \quad \big]. \tag{5}$$

H. Optimization

To find optimal parameter sets a two-step optimization procedure is conducted. First, the mechanisms are optimized towards a high balancing quality, i.e., to minimize the error $\boldsymbol{\delta}$ as defined in Equation (3). In the second step, this error is limited to $\boldsymbol{\delta} \leq 0.05$, while the relative strength of the mechanism is optimized towards a maximum value of $\boldsymbol{\epsilon}$ as defined in Equation (4). With the exception of the redefinition of $\boldsymbol{\delta}$ from objective to constraint, both optimizations are subject to the same set of bounds and constraints. The constraints are implemented as inequality constraints, denoted $\mathbf{c}$, and soft constraints, i.e., penalties $\mathbf{p}$. The inequality constraints $\mathbf{c}$ are evaluated for the initial mechanism state, before running the SPACAR simulation. If any of these produce a value > 0, the simulation is skipped and an error value returned. The penalties $\mathbf{p}$, similar to the objectives $\boldsymbol{\delta}$ and $\boldsymbol{\epsilon}$, are evaluated after the simulation. Their values are multiplied with a penalty factor $k_p = 10^5$ and added to the cost function.

The two cost functions can be written as:

$$f_1(\mathbf{x}) = \boldsymbol{\delta} + k_p \mathbf{p}_{(1-6)} \tag{6}$$

$$f_2(\mathbf{x}) = \frac{1}{\boldsymbol{\epsilon}} + k_p \mathbf{p}_{(1-7)} \\ \text{subject to} \quad \mathbf{c}_{(1-7)} \leq 0 \tag{7}$$

The first two constraints $\mathbf{c}_{(1)}$ and $\mathbf{c}_{(2)}$ check whether the arm is pointing upwards with a maximum deviation of $\alpha = \frac{\pi}{9}$ from vertical.

$$\mathbf{c}_{(1)} = \cos(\theta_{init}) \tag{8}$$

$$\mathbf{c}_{(2)} = |\sin(\theta_{init})| - sin(\alpha) \tag{9}$$

where θ_{init} is the initial angle of the arm link.

The next two constraints $\mathbf{c}_{(3)}$ and $\mathbf{c}_{(4)}$ check, whether the flexure attaches to the upper arm within a specified distance range $\text{ł} = [0.05 \cdots 0.3]$ m from the shoulder.

$$\mathbf{c}_{(3)} = \text{ł}_{min} - \text{ł} \tag{10}$$

$$\mathbf{c}_{(4)} = \text{ł} - \text{ł}_{max} \tag{11}$$

where ł is the length of the arm link, i.e., of the respective beam element in the SPACAR model.

For the constraint $\mathbf{c}_{(5)}$ a self-intersection test is performed on the flexure. To this end, each line segment, given by the end nodes of the beam elements constituting the flexure, is checked for intersections with all other line segments. This procedure, which is described in detail in [25], yields the total number of self-intersections $\mathsf{n}_{\times}$.

$$\mathbf{c}_{(5)} = \mathsf{n}_{\times} \tag{12}$$

Constraint $\mathbf{c}_{(6)}$ determines whether the beam penetrates either the torso or the arm mesh. Each contact node j is assigned a value of $\mathsf{n}_{\in} = 1$, if it lies within at least one of the two meshes, and $\mathsf{n}_{\in} = 0$, if not. The sum of $\mathsf{n}_{\in}$ for all contact nodes yields the constraint value.

$$\mathbf{c}_{(6)} = \sum_{j=0}^{m} \mathsf{n}_{\in \mathrm{j}} \tag{13}$$

Analogously, the constraint $\mathbf{c}_{(7)}$ determines whether the beam lies outside both offset meshes. Each contact node is assigned a value of $\mathsf{n}_{\notin} = 1$, if it lies outside both the torso and arm offset mesh, and $\mathsf{n}_{\notin} = 0$, if not. However, in the scope of this constraint only the first four contact nodes of the beam element at the back interface are checked, to ensure the flexure starts within the protrusion limit.

$$\mathbf{c}_{(7)} = \sum_{j=0}^{4} \mathsf{n}_{\notin \mathrm{j}} \tag{14}$$

The first three penalties directly correspond to the constraints $\mathbf{c}_{(3)}$, $\mathbf{c}_{(4)}$ and $\mathbf{c}_{(5)}$, whereby the respective constraint values are evaluated for each load step i and added in case they are positive. Penalties $\mathbf{p}_{(1)}$ and $\mathbf{p}_{(2)}$ shall prevent the interface point from sliding outside the specified range from the shoulder, when the arm link acts as a slider.

$$\mathbf{p}_{(1)} = \sum_{i=0}^{n} \text{ł}_{min} - \text{ł}_i \qquad \forall \qquad \text{ł}_{min} - \text{ł}_i > 0 \tag{15}$$

$$\mathbf{p}_{(2)} = \sum_{i=0}^{n} \text{ł}_i - \text{ł}_{max} \qquad \forall \qquad \text{ł}_i - \text{ł}_{max} > 0 \tag{16}$$

Penalty $\mathbf{p}_{(3)}$ shall prevent self-intersections throughout the full deformation range of the flexure.

$$\mathbf{p}_{(3)} = \sum_{i=0}^{n} \mathsf{n}_{\times \mathrm{i}} \tag{17}$$

Penalties $\mathbf{p}_{(4)}$ and $\mathbf{p}_{(5)}$ are an extension to the constraints $\mathbf{c}_{(6)}$ and $\mathbf{c}_{(7)}$. In addition to evaluating whether a node lies within the torso and arm mesh or outside the offset meshes, the penetration depth and protrusion distance are evaluated for each respective node, as to provide a more continuous change in the cost function. For both $\mathbf{p}_{(4)}$ and $\mathbf{p}_{(5)}$ this evaluation is carried out for all contact nodes. However, while the penetration depth is considered for the entire range of motion, the protrusion is only taken into account for the lower elevation angles $\theta \leq \frac{\pi}{2}$ which are most critical for ADLs [33].

$$\mathbf{p}_{(4)} = \sum_{i=0}^{n} \sum_{j=0}^{m} \left| d_{i,j} \right| \qquad \forall \qquad \mathsf{n}_{\in \mathrm{i,j}} = 1 \tag{18}$$

$$\mathbf{p}_{(5)} = \sum_{i=n/2}^{n} \sum_{j=0}^{m} d_{i,j} \qquad \forall \qquad \mathsf{n}_{\notin \mathrm{i,j}} = 1 \tag{19}$$

where d is the shortest distance to either the torso or the arm mesh and index j denotes each contact node. By convention, d is signed negative when pointing inside the mesh and positive when pointing outside.

The last regular penalty $\mathbf{p}_{(6)}$ returns the value by which the von Mises stress exceeds the stress limit σ_{lim}. The von Mises stress in each beam element constituting the flexure is determined for each load step, and the highest overall value is assigned to σ_{Mises}.

$$\mathbf{p}_{(6)} = \begin{cases} 0, & \text{if } \sigma_{Mises} - \sigma_{lim} \leq 0 \\ \sigma_{Mises} - \sigma_{lim}, & \text{if } \sigma_{Mises} - \sigma_{lim} > 0 \end{cases} \tag{20}$$

$$\sigma_{lim} = \frac{\sigma_t}{FOS} \tag{21}$$

where σ_t is the tensile stress of the flexure material and $FOS = 1.2$ the applied factor of safety.

As stated previously, the objective $\boldsymbol{\delta}$ of the first optimization is turned into a penalty for the second optimization. To this end, a conditional extra penalty $\mathbf{p}^*_{(7)}$ applies only during that second optimization.

$$\mathbf{p}^*_{(7)} = \begin{cases} 0, & \text{if } \boldsymbol{\delta} - \delta_{lim} \leq 0 \\ \boldsymbol{\delta} - \delta_{lim}, & \text{if } \boldsymbol{\delta} - \delta_{lim} > 0 \end{cases} \tag{22}$$

where $\delta_{lim} = 0.05$ is the limit on the gravity balancing error.

The two cost functions $f_1(\mathbf{x})$ and $f_2(\mathbf{x})$ are optimized sequentially using the *particleswarm()* solver from the MATLAB Global Optimization Toolbox, whereby the optimized parameter set of the first optimization serves as the initial point for the second optimization.

I. Investigation Scheme

Using this optimization routine, mechanism designs for every feasible combination of support conditions are optimized. First, all combinations of support conditions are investigated which feature either only approximately zero or infinite stiffness at each joint. Hence, no joint stiffness parameters are optimized. However, since these designs rely on storing all their energy in the flexure, only designs with a mobility of the flexure of ≤ 0 are considered. Consequently, combinations with ≥ 3 degrees of freedom and with two sliders are excluded. The latter is due to the kinematic singularity that occurs when both sliders are parallel. This leaves 10 feasible out of 16 possible combinations.

Next, all combinations of support conditions are investigated for which a stiffness parameter is assigned to each released joint, i.e., when considering only a non-zero finite or infinite stiffness at each joint. Each assigned stiffness parameter becomes part of the parameter set, and thus is optimized along with the flexure shape. In this case no mobility issues arise, making all combinations feasible. However, since the case with infinite stiffness in all joints is already covered only 15 additional combinations are considered, making it in total 25 different support conditions that are investigated. An overview of the investigated support conditions is given in Table I.

For each of the different support conditions the optimization routine is conducted at least 51 times, and on average 65 times. Between each individual optimization trial the maximum allowed protrusion, affecting the offset mesh and thus penalty $\mathbf{p}_{(5)}$, is alternated between the values $o = [75, 100, 150]$ mm. Based on this broad investigation the combinations of support conditions that yield feasible results are identified.

These feasible mechanisms are subsequently categorized regarding their apparent support conditions at each interface,

TABLE I
OVERVIEW OF FEASIBLE SUPPORT CONDITIONS

			Back			
			Clamp	Hinge	Slider	Slider/ Hinge
		DOF	0	1	1	2
Arm	Clamp	0	✓	✓	✓	✓
	Hinge	1	✓	✓	✓	(✓)*
	Slider	1	✓	✓	(✓)*	(✓)*
	Slider/Hinge	2	✓	(✓)*	(✓)*	(✓)*

$\star$: only feasible with a non-zero stiffness in at least one joint

and for each category two representative designs are chosen and dimensioned. PA2200 with a Young's modulus of $E = 1.7$ GPa, a tensile stress of $\sigma_t = 50$ MPa and a density of $\rho = 930$ kg/m^3 is used as flexure material, and the maximum flexure thickness is limited to 25 mm. By adjusting the flexure width and joint stiffnesses, a moment amplitude of 10 Nm is set for every example mechanism. This provides a comparison between the different categories of feasible mechanisms.

Subsequently, two promising categories featuring distinct support conditions are selected for further investigation. These are re-optimized using custom settings in order to obtain more refined flexure mechanism designs which serve as the basis for the physical prototypes that are experimentally evaluated.

III. EXPERIMENT

Following the investigation scheme, physical prototypes for the two improved flexure mechanism designs, labeled **A** and **B**, are made and tested on a dedicated test bench. The test bench is designed to emulate the conditions in the simulation, and thereby validate both the angle-dependent stiffness behavior and the alignment with the body. Due to the different support conditions which affect the physical interfaces between the flexure and the test bench, prototype **A** and prototype **B** require different test bench configurations. The test bench as configured for prototype **B** can be seen in Figure 2, while the configuration for prototype **A** is shown in the *Results* section in the left column of Figure 6. For the structural components 40x40 mm aluminum profiles and 3 mm steel plate are used, while a 25 mm thick aluminum plate serves as the base. The tested flexure prototypes, the arm and torso shells, as well as the hub of the shuttle assembly are made from laser-sintered PA2200. Due to size limitations imposed by the laser sintering machine both flexures are split into two parts.

The arm consists of two parallel steel plates to which two shells with mounting holes are attached. At the distal end both plates are connected, and an adjustable balance weight is fixed to set the moment amplitude. The weight can be shifted to align the arm's center of gravity with the arm axis. At the proximal end both plates are connected to a timing pulley which is mounted to the top of a pole via two ball bearings. Below the pole a second timing pulley is located and fixed to the output of a Neugart PLE080 gearbox which is driven by a Kollmorgen AKM22C motor. The motor is powered and controlled via a Kollmorgen S20260-VTS servo drive. Opposite to the gearbox a YUMO E6B2-CWZ3E digital quadrature encoder is connected to the same output through a bellows coupling. Both timing pulleys are connected via an open timing belt. The belt is clamped to the lower pulley, runs over the top pulley and extends back down where it connects to an adjustable counterweight. In between the two pulleys the belt is interrupted by an assembly consisting of two clamps and a ME-Meßsysteme KM26z load cell. The signals from the load cell are amplified by a ME-Meßsysteme GSV-11H 010-5/20/2

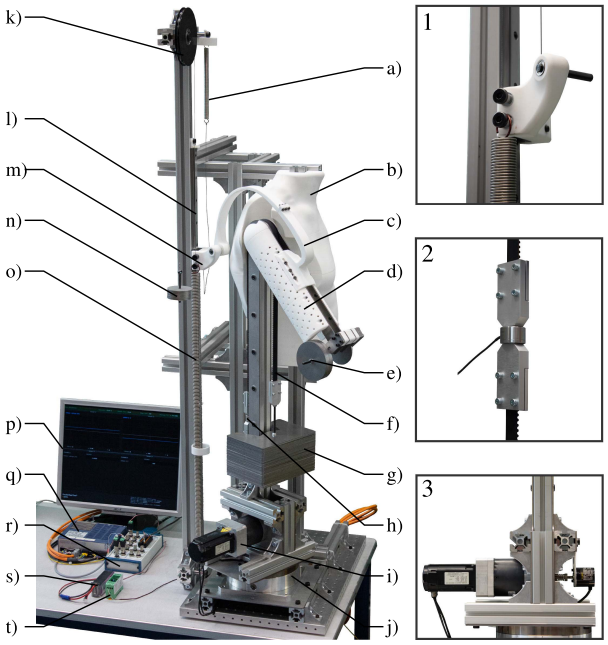

Fig. 2. Experimental setup, configuration **B**. a) secondary spring (connected to the shuttle via a string), b) torso shell, c) flexure specimen (prototype **B**), d) arm shell, e) balance weight, f) timing belt, g) counterweight, h) force sensor assembly, i) actuator (motor and gearbox), j) rotary stage, k) pulley, l) linear guide, m) shuttle assembly, n) shuttle counterweight, o) primary spring, p) Simulink Real-Time scope, q) motor driver, r) NI adapter, s) battery, t) measuring amplifier. Detail 1: shuttle assembly without specimen; Detail 2: force sensor assembly; Detail 3: auxiliary view showing the position of the encoder, connected to the actuator output via a bellows coupling.

measuring amplifier, using a battery for power supply. The entire assembly rests on a rotary stage, that can be used to set the horizontal flexion/extension angle γ. A separate frame serves as the mount for the prototype's back interfaces and the torso reference shell.

Prototype **A** has a mechanism design in which the flexure is clamped to the back and which connects via a zero-stiffness hinged interface to the arm. It consists of three major parts. The first part of the flexure containing the back interface is simply bolted to the frame. It is connected to the second part of the flexure via a flange, which is bolted and reinforced with instant adhesive. At its other end, the second part of the flexure is mounted via a shaft to a ball bearing which is contained in the arm interface. This hinged interface in turn is bolted to the arm shells via two slotted holes.

Prototype **B**, shown in Figure 2, is based on a design in which the flexure connects via a zero-stiffness hinge to a slider with non-zero stiffness at the back and which is clamped to the arm. Hence, it features a more complex design. A shuttle which incorporates a sliding block, bolts for connecting springs and counterweights, as well as a shaft supported by two ball bearings, constitutes the back interface of this design. The sliding block runs in a linear track, which is fixed to a long aluminum profile that is attached to the frame. To set the bi-directional stiffness of the translational degree of freedom two tension springs are used. The main spring covers most of the range of motion and is fixed between the lower end of the aluminum profile and the shuttle. The secondary spring is suspended from the top of the profile and connected to the shuttle via a string which disengages the spring when not in use. In addition to the springs, another string connects the shuttle to a counterweight, which is suspended from a pulley at the top of the aluminum profile. It is used to adjust the effective weight of the shuttle assembly to the value set in simulation. The

first part of the flexure is fixed to the shaft of the shuttle and connects to the second part of the flexure in the same way as prototype **A**. That second part containing the arm interface is then directly fixed to the arm shells.

The entire setup is controlled and the sensor readings obtained via Simulink Real-Time. To this end, a PC with a National Instruments PCI-6221 multifunction I/O card and a National Instruments BNC-2110 adapter are used. During experiments the arm is raised from the lowest position $\theta = 0$ to the raised position $\theta = \pi$, and lowered back to the lowest position using a constant speed. The signals are acquired at a rate of 100 Hz and the force signal is filtered using a moving average filter with a window size of 20 samples. Each configuration is measured with and without the flexure. The two measurements are then subtracted from each other to isolate the mechanical behavior of the flexure mechanism. Multiplying the force data with the partial diameter of the timing pulley at the arm yields the shoulder moment. In the absence of an absolute zero reference for the force signal, the moment offset is adjusted such that the zero crossing for the unstressed state at which the mechanism is assembled matches the simulation.

IV. Results

A total number of 1616 optimizations is conducted, resulting in 204 feasible mechanism designs. These are found for 18 of the 25 investigated support conditions. All support conditions yield feasible results for non-zero finite joint stiffnesses. However, only three achieve a balancing behavior below the threshold of NMEA ≤ 0.05 when using zero stiffness in all released joints. Each of the feasible mechanisms is categorized by its apparent support conditions based on the kinematic behavior as identified through the amount of displacement displayed at each interface joint. Accordingly, the label *Clamp*, *Slider*, *Hinge* or *Slider/Hinge* is assigned to each interface. Thereby, 10 feasible categories of mechanisms are found that correspond to the 16 possible kinematic combinations shown in Table I. The other 6 kinematic combinations are avoided in optimization by assigning high stiffnesses to some of the released joints. Consequently, these joints display no significant motion, making them behave as if rigid.

Out of each feasible category two designs are chosen as representative examples, and are dimensioned for an amplitude of 10 Nm. Animations of these two examples, labeled 1 and 2, for each category can be seen in Figure 3. The categories are named by first stating the condition at the arm interface and then, separated by a dash, at the back interface. The three kinematic categories that work without using non-zero finite stiffnesses, i.e., springs are the first three shown in the first column of Figure 3. They feature either two clamped interfaces, or one clamped and one hinged interface. The chosen examples for these three categories all feature approximately zero stiffness in the joints. All other categories require non-zero finite joint stiffnesses in order to work. Some rely solely on the interfaces for their function, reducing the flexure to a structural element. An example for this is the *Slider/Hinge–Hinge* category in which both designs resemble the inverse slider-crank mechanism described by Kim *et al.* [37].

The *Hinge–Clamp* and the *Clamp–Slider/Hinge* categories are chosen for further investigation. Design **A** is obtained by re-optimizing the *Hinge–Clamp* category with zero hinge stiffness. This category is chosen, since it offers the lowest protrusion and best relative strength among the categories that only utilize the flexure for energy storage, which may offer a lower complexity and smaller number of parts in comparison to categories which require spring loaded interfaces. For **B** the *Clamp–Slider/Hinge* category is chosen as this category offers the best theoretical performance across all designs that still make significant use of the flexure for energy storage. Furthermore, the fashion in which the flexure aligns to the body as well as the low reaction forces and moments at the interfaces make this design appear very advantageous despite its increased design complexity. To mitigate the design complexity the stiffness of the back hinge is set to zero, while a constant stiffness of 100 N/m is assigned to the back slider, during re-optimization.

A comparison between the computed performance metrics of the prototypes and the two examples of each kinematic category is given in Table II. Since the mechanisms in this study are all designed for a moment amplitude of 10 Nm, the relative shear force represents 10 % of the absolute maximum shear force. Graphs showing the optimized angle-dependent balancing behavior for **A** and **B** are shown in Figure 4. Corresponding graphs for all other examples are provided in supplementary file 1. The construction parameters for the flexures employed in **A** and **B** are given in Table III in the Appendix. Corresponding tables for all other examples along with information about the joint stiffnesses and ranges of motion are provided in supplementary file 2. Table IV in the Appendix shows the energy distribution between the flexure and the individual joints at $\theta = 0$. Movies showing the full animations of all simulated mechanisms shown in juxtaposition to the balancing graphs are provided in supplementary file 3.

The prototypes for **A** and **B** are accidentally dimensioned only on basis of the stresses at the last load step. Consequently, they surpass the stress limit by 1.9 MPa and 10.8 MPa, respectively, when considering the entire range of motion. This did not lead to failure or any observed negative consequences. However, to provide an accurate comparison with the other examples, corrected values for beam dimensions observing the stress limit are given in brackets in Tables II and III.

The results of the measurements performed at $\frac{\pi}{60}$ rad/sec are shown in Figure 5. The animations of **A** and **B** in juxtaposition to photographs of the experiment are shown in Figure 6. Corresponding movies showing the full animation and photo time lapse alongside the respective graphs are provided in supplementary files 4 and 5. Movies showing the experiment of **A** and **B** from several different angles are provided in supplementary files 6 and 7.

V. Discussion

A large variety of distinct mechanism designs was found that fulfill both the requirements regarding gravity balancing and collision avoidance. These can be categorized into kinematic categories based on their apparent support conditions as shown in Figure 3, but also by the way they achieve gravity balancing and by the degree to which they utilize the flexure.

When considering the force and moment at the arm interface, as can be seen in Figure 3, there are three ways of achieving gravity balancing. Mechanisms that feature no significant moment at the arm interface can only utilize the interface force for balancing. At the raised position the interface force is small, but has a large lever arm with respect to the shoulder joint. As the arm moves down the force increases while the lever arm decreases, creating the sine-shaped moment at the shoulder joint. At the lowest position the force points directly at the shoulder joint to achieve

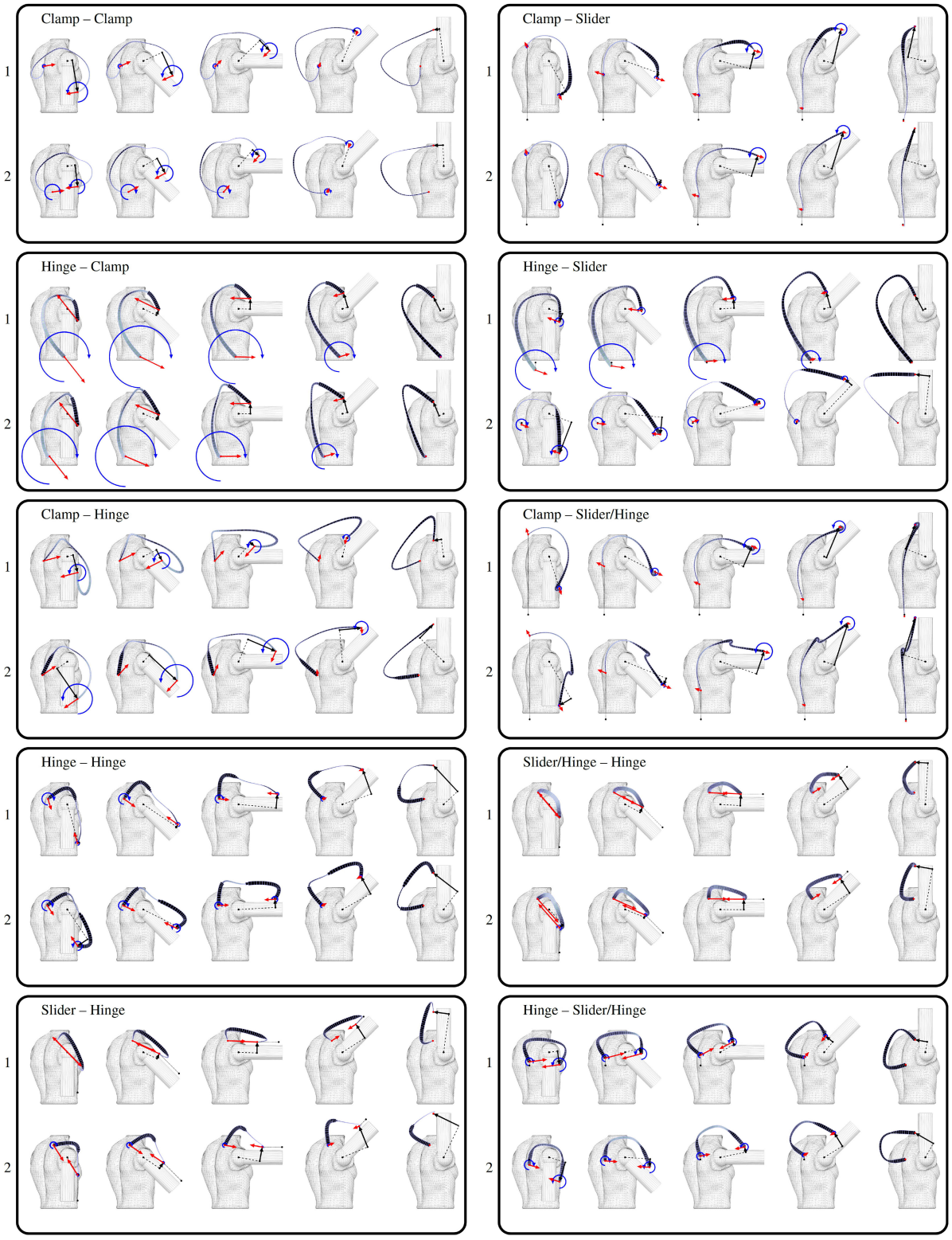

Fig. 3. Animations of the example mechanisms arranged by kinematic category. Red arrows are proportional to reaction forces (1 mm/N), the blue arrow's radii to reaction moments (33 mm/Nm). Black arrows depict the lever arm of the arm interface force with respect to the shoulder joint, marked by a dot. A perpendicular dashed line connects the lever arm arrow and shoulder joint. Dotted lines show slider displacements from the initial positions marked by dots.

a zero moment. Examples for this behavior are the categories *Hinge–Clamp*, *Slider–Hinge* and *Slider/Hinge–Hinge*. As for their functioning the force vector has to stay mostly parallel to the arm, these three categories feature larger relative shear forces than all other categories. Mechanisms that feature a progressively increasing arm interface moment towards lower angles have to use the arm interface force to counteract it. As the interface force is also progressively increasing, its lever arm with respect to the shoulder joint has to change in such a manner that the moment caused by the interface force subtracted from the interface moment results in the desired sine-shaped angle-to-moment relation at the

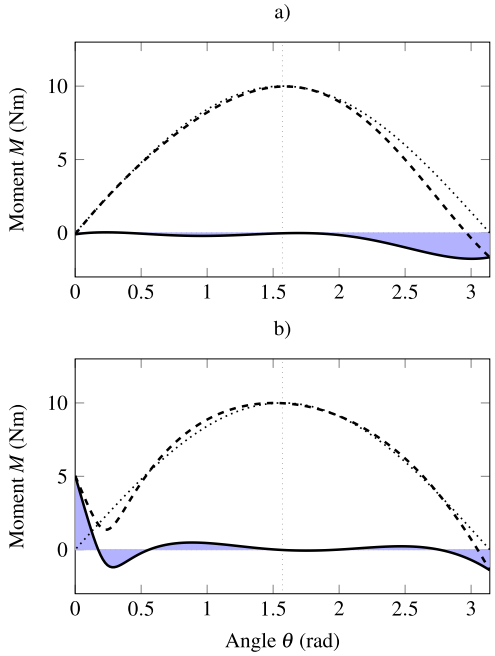

Fig. 4. Optimized balancing behavior of (a) **A** and (b) **B**. The dashed line depicts the computed moment generated by the mechanism. The dotted line shows the ideal characteristic, i.e., the inverse of the load moment. The solid line shows the balanced behavior of the mechanism, when adding the load moment to the mechanism's moment. The shaded areas indicate the balancing error. This diagram shows good balancing behavior for both prototypes throughout the range of motion. **A** shows progressively imbalanced behavior towards the raised position, while **B** shows a sudden deviation at smaller angles.

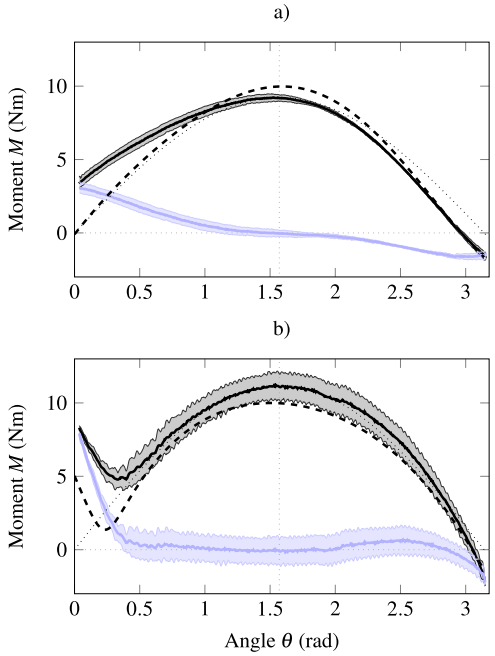

Fig. 5. Experimental results for (a) prototype **A** and (b) prototype **B**. The thin black solid line depicts the measured moment exerted by the mechanism. The thick black solid line depicts the mean and the shaded area in between indicates the hysteresis. A sine curve matching the maximum amplitude of the measured mean is depicted by the black thin dotted line. The balanced moment characteristic, i.e., the difference between the sine curve and measured data, is analogously depicted in light blue. The corresponding simulation result is shown by the dashed line. In comparison to the computed results, prototype **A** shows additional progressively imbalanced behavior towards smaller angles. For prototype **B** the sudden deviation from balanced behavior at smaller angles occurs earlier. Furthermore, both results show a mismatch in amplitude of -0.78 Nm and $+1.2$ Nm for **A** and **B**, respectively. Prototype **B** exhibits significantly more hysteresis than prototype **A**.

TABLE II
PERFORMANCE METRICS

		Balancing Error δ	Relative Strength ϵ	Maximum Protrusion	Relative Shear Force
		-	Nm/cm	cm	N/Nm
A *Hinge–Clamp*		0.0440 (0.0440)	2.58 (2.27)	18.40 (18.51)	-16.63 (-16.63)
B *Clamp–Slider/Hinge**		0.0435 (0.0434)	3.33 (1.68)	9.96 (11.02)	+6.61 (+6.65)
Clamp–Clamp	1	0.0419	1.23	29.15	-4.54
	2	0.0433	0.94	29.69	-4.22
Hinge–Clamp	1	0.0413	5.11	17.03	-18.29
	2	0.0454	3.77	20.62	-16.56
Clamp–Hinge	1	0.0462	3.43	21.59	-6.57
	2	0.0455	1.98	26.71	+6.39
Hinge–Hinge*	1	0.0410	4.34	21.03	-9.67
	2	0.0443	5.50	19.67	-8.78
Slider–Hinge*	1	0.0500	1.60	11.63	-17.74
	2	0.0511	0.34	22.61	-11.34
Clamp–Slider*	1	0.0574	0.74	14.71	+5.93
	2	0.0723	0.94	13.53	+6.09
Hinge–Slider*	1	0.0495	8.39	21.43	-8.46
	2	0.0443	1.45	35.14	-5.06
Clamp–Slider/Hinge*	1	0.0392	1.96	12.26	+5.84
	2	0.0379	1.36	12.91	+5.66
Slider/Hinge–Hinge*	1	0.0401	28.94	10.62	-16.86
	2	0.0417	25.1	11.24	-16.77
Hinge–Slider/Hinge*	1	0.0377	8.73	13.98	-9.48
	2	0.0372	21.85	19.85	-7.39

*feasible results obtained only for finite non-zero stiffness values.

shoulder joint. This typically results in the force vector orienting itself perpendicular towards the arm at lower elevation angles. Examples for this are the categories *Clamp–Clamp*, *Clamp–Hinge*, *Hinge–Slider* and *Hinge–Slider/Hinge*. Lastly, a group of mechanisms exist that feature an arm interface moment that first increases as the arm is lowered from the raised position towards the horizontal position, but decreases again as it is further lowered. Thus gravity balancing can be achieved without a major contribution from the arm interface force. For this type of behavior the location of the back interface has to change significantly. Consequently, a slider with large stroke at the back is required. Examples for this are the *Clamp-Slider* and *Clamp-Slider/Hinge* categories. These mechanisms feature the lowest interface forces.

When considering the energy distribution shown in Table IV the mechanisms can, again, be divided into three different types. The first type uses only the flexure for energy storage. It corresponds to the three categories *Clamp–Clamp*, *Hinge–Clamp* and *Clamp–Hinge* for which results were found, when only zero joint stiffnesses are applied. The second type is a hybrid which uses both the flexure and interfaces for storing energy. Mechanisms of this type feature up to two joints, of which one is used for energy storage. They belong to the categories *Clamp–Slider*, *Hinge–Slider* and *Clamp–Slider/Hinge*. The third type nearly exclusively uses the joints for energy storage. In these cases the flexure is reduced to a means of transmission. For that reason this type was not considered for further investigation in this study. This pertains to the categories *Hinge–Hinge*, *Slider–Hinge*, *Slider/Hinge–Hinge* and *Hinge–Slider/Hinge*.

Prototype **A** offers a relatively low complexity and a small number of parts. In comparison to the *Clamp–Clamp* and *Clamp–Hinge* categories which also feature zero-stiffness joints it shows the best potential for close-to-body alignment

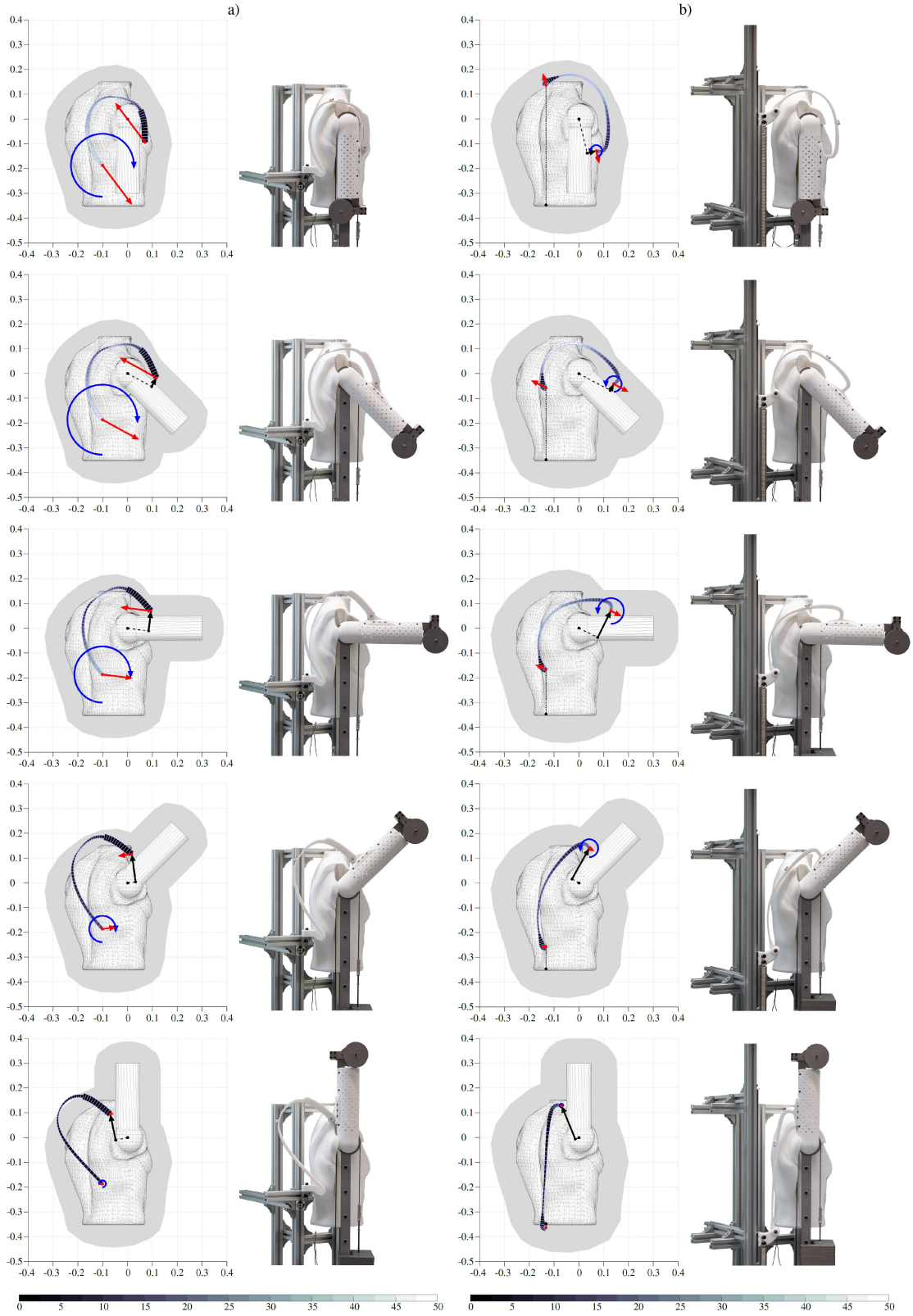

Fig. 6. Juxtaposition of animations and photographs from the experiment of (a) **A** and (b) **B**. Axes are in m, color scale in MPa. The remaining description of the animations is equal to Figure 3. The shuttle counterweight and secondary spring are removed from (b) as not to obstruct the view on the flexure.

and relative strength. Though the maximum protrusion is relatively high, it drops steadily from 18 cm at $\theta = \pi$, below 10 cm at $\theta = \frac{\pi}{2}$, and down to 6 cm at $\theta = 0$. However, the large shear force at the arm and very large moment at the back interface are the two main disadvantages of this design. In addition, the experiments indicate that purely force-based gravity balancing may be more sensitive to disturbances. Due to the small lever arm the orientation of the force vector with respect to the shoulder has to be very precise in order to function properly. The results indicate that with increasing

stress and deformation in the system, this may be hard to achieve causing the progressive deviation between simulation and experiments towards smaller angles, as shown in Figure 5. Therefore, in retrospect, the *Clamp–Hinge* category may be the better choice out of the three categories that exclusively use the flexure for energy storage.

As one of the hybrid types prototype **B** is more complex, but offers the best theoretical performance out of all designs that make use of the flexure for energy storage. In addition, its close alignment with the body and the low interface forces and moments are key advantages. In comparison to **A** the protrusion remains more steady, dropping from 10 cm at $\theta = \pi$, down to 7 cm for the range between $\theta = 2$ to $\theta = 0.5$, and going back up to 10 cm at $\theta = 0$. In comparison to the very similar *Clamp-Slider* category the additional hinge at the back yields performance gains throughout all metrics. By observation of the energy distribution and stiffnesses, it was concluded that for this prototype design predefined stiffness values can be assigned to the joints. Thereby, the search space for the optimization was reduced and the construction simplified. Considering the measurement data shown in Figure 5 the balancing behavior seems more robust than that of prototype **A**, showing larger qualitative divergence only at angles below 0.5 rad. At these smaller angles also a positional deviation of the back interface between simulation and experiment occurs, as can be seen in Figure 6. However, this could be in part caused by the missing counterweight.

All mechanisms found in this study exhibit a maximum protrusions of at least 10 cm. Hence, modifications to the synthesis method are likely required to further improve the alignment with the body and reduce protrusion. The joint-centric designs may be improved by replacing the flexure element by a structure or mechanism which aligns laterally to the body, as is done in the ShoulderX [22] which shares similarities with the *Slider/Hinge–Hinge* designs.

For the flexure-based designs the *Clamp–Slider/Hinge* category seems to offer the best prospects. Potential ways of improving the alignment to the body may include the investigation of nonlinear tracks for the slider that conform better to the body, active guidance of the flexure, e.g., with rollers, allowing contact with the body, as well as the investigation of spatial flexure designs that connect laterally to the arm. In addition, a vertical pivot for horizontal flexion/extension will likely be required. Also, though the compliance of the mechanical structure appears to offer a certain degree of self-adaptability and thus tolerance with respect to misalignment between the mechanism and the shoulder, the effect of scapulothoracic motion on the performance needs to be evaluated.

In comparison to the rigid-link devices which are mentioned in Section I the test-bench prototypes presented in this study are still very preliminary. A technical comparison is difficult, since the performance metrics used in this study are not or only partially available for those devices. Also, due to the lack of suitable wearable prototypes, an evaluation on basis of the reduction in muscle activation during manual tasks – a measure typically used for the other devices – could not be performed. Generally, it can be stated that current rigid-link devices are able to achieve similar levels of gravity compensation quality and quantity as well as protrusion, and furthermore avoid shear forces at the arm attachment – often through the use of linear guides. Hence, the key advantage of the mechanisms presented in this paper remains their inherent compliance. This, in the future, may provide improved self-adaptability and allow for close contact with the user, thus potentially offering better wearing comfort and significantly reduced conspicuity.

TABLE III
FLEXURE PARAMETERS

Parameter	Unit	**A**		**B**	
s_x	mm	-101.4		-132.6	
s_z	mm	-186.4		-346.6	
l_1	mm	309.6		13.5	
l_2	mm	127.8		468	
l_3	mm	155.2		42.4	
φ_1	rad	2.145		2.666	
φ_2	rad	0.9105		1.4635	
φ_3	rad	-0.4639		0.2735	
t_1	mm	12.5	(12)	47.9	(38.1)
t_2	mm	11	(10.6)	5.2	(4.2)
t_3	mm	4.4	(4.2)	8	(6.3)
t_4	mm	12.9	(12.4)	16.1	(12.8)
t_5	mm	197.6	(189.4)	12.2	(9.7)
w	mm	38.7	(44.1)	30	(59.5)

TABLE IV
ENERGY DISTRIBUTION AT $\theta = 0$ ON A PERCENTAGE BASIS

		Flexure	Arm		Back	
			Slider	Hinge	Slider	Hinge
A *Hinge–Clamp*		100		0		
B *Clamp–Slider/Hinge*		39			61	0
Clamp–Clamp	1	100				
	2	100				
Hinge–Clamp	1	100		0		
	2	100		0		
Clamp–Hinge	1	100				0
	2	100				0
Hinge–Hinge	1	4		13		83
	2	5		25		71
Slider–Hinge	1	10	87			3
	2	15	46			39
Clamp–Slider	1	56			44	
	2	61			39	
Hinge–Slider	1	42		55	4	
	2	36		63	1	
Clamp–Slider/Hinge	1	38			61	0
	2	36			61	3
Slider/Hinge–Hinge	1	8	87	0		4
	2	10	72	10		7
Hinge–Slider/Hinge	1	6		64	1	29
	2	6		46	2	46

In preparation to this study contact with the body and spatial flexure designs have already been investigated. However, the high computational cost for the contact analysis and the largely increased search space when considering additional bending and torsion deformation angles of the flexure were reasons to exclude these aspects from this study.

VI. CONCLUSION

This study aimed to find close-to-body gravity-balancing flexure-based mechanisms for shoulder support that may be used without any additional rigid linkages between the torso and the arm. A broad optimization study into different kinematic support conditions revealed a multitude of possible designs – many of which are left for further investigation.

Of the two designs that were developed into prototypes and evaluated in experiment both show good gravity balancing behavior. Prototype **A** reduces the required maximum moment to lift the arm by more than 80 % over the entire simulated, and 85 % of the measured range of motion. Prototype **B** shows even better balancing qualities, offering the same more-than-80% reduction over 97 % of the simulated, and 92 % of the measured range of motion. In addition, design **B**, having the lowest protrusion out of all flexure-based designs, features a maximum protrusion that is 46 % less than that of design **A**. Furthermore, the low interface forces and moments

of design **B**, which are over 60 % lower compared to design **A**, are potential key enablers for a fully compliant exoskeleton structure. Therefore, a design with a tapered flexure which on one end connects via a hinge to a slider at the back, and on the other end is clamped to the upper arm appears to be the most promising solution for the proposed exoskeleton architecture.

Though it seems feasible that in terms of size and protrusion the current design **B** could already compete with the mechanisms employed in commercially available shoulder supports, the device is still far from the aspired 3 cm distance to the body. Possible leads to mitigate this shortcoming in future work are provided. Aside from this, however, additional work will be necessary to translate the test bench prototype mechanism into a wearable assistive device. To this end, better integration, simplification and customization of all components will be the main challenges.

APPENDIX
TABLES

See Tables III and IV.

ACKNOWLEDGMENT

The content of this publication is the sole responsibility of the authors. The European Commission or its services cannot be held responsible for any use that may be made of the information it contains.

REFERENCES

[1] L. A. van der Heide, B. van Ninhuijs, A. Bergsma, G. J. Gelderblom, D. J. van der Pijl, and L. P. de Witte, "An overview and categorization of dynamic arm supports for people with decreased arm function," *Prosthet. Orthot. Int.*, vol. 38, no. 4, pp. 287–302, 2014.

[2] A. G. Dunning and J. L. Herder, "A review of assistive devices for arm balancing," in *Proc. IEEE 13th Int. Conf. Rehabil. Robot. (ICORR)*, 2013, pp. 1–6.

[3] T. McFarland and S. Fischer, "Considerations for industrial use: A systematic review of the impact of active and passive upper limb exoskeletons on physical exposures," *IISE Trans. Occup. Ergonom. Human Fact.*, vol. 7, nos. 3–4, pp. 322–347, 2019.

[4] P. Maciejasz, J. Eschweiler, K. Gerlach-Hahn, A. Jansen-Troy, and S. Leonhardt, "A survey on robotic devices for upper limb rehabilitation," *J. NeuroEng. Rehabil.*, vol. 11, no. 1, p. 3, 2014.

[5] S. K. Manna and V. N. Dubey, "Comparative study of actuation systems for portable upper limb exoskeletons," *Med. Eng. Phys.*, vol. 60, pp. 1–13, Oct. 2018.

[6] R. J. Varghese, D. Freer, F. Deligianni, J. Liu, and G.-Z. Yang, "Wearable robotics for upper-limb rehabilitation and assistance: A review of the state-of-the-art, challenges and future research," in *Wearable Technology in Medicine and Health Care*, R. K.-Y. Tong, Ed. Cambridge, MA, USA: Academic Press, 2018, ch. 3, pp. 23–69.

[7] A. J. Veale and S. Q. Xie, "Towards compliant and wearable robotic orthoses: A review of current and emerging actuator technologies," *Med. Eng. Phys.*, vol. 38, no. 4, pp. 317–325, 2016.

[8] P. N. Kooren *et al.*, "Design and pilot validation of A-Gear: A novel wearable dynamic arm support," *J. NeuroEng. Rehabil.*, vol. 12, no. 1, p. 83, 2015.

[9] J. Hull, R. Turner, A. A. Simon, and A. T. Asbeck, "A novel method and exoskeletons for whole-arm gravity compensation," *IEEE Access*, vol. 8, pp. 143144–143159, 2020.

[10] J. Chen and P. S. Lum, "Pilot testing of the spring operated wearable enhancer for arm rehabilitation (SpringWear)," *J. NeuroEng. Rehabil.*, vol. 15, no. 1, p. 13, 2018.

[11] (Ekso Bionics, Richmond, CA, USA). *EksoVest, EksoUE & EVO*. Accessed: Mar. 5, 2022. [Online]. Available: eksobionics.com

[12] (JAECO Orthopedic, Hot Springs, AR, USA). *Wilmington Robotic Exoskeleton (WREX)*. Accessed: Mar. 5, 2022. [Online]. Available: jaecoorthopedic.com

[13] T. Haumont *et al.*, "Wilmington robotic exoskeleton: A novel device to maintain arm improvement in muscular disease," *J. Pediatr. Orthop.*, vol. 31, no. 5, pp. e44–e49, 2011.

[14] (Levitate Technol., San Diego, CA, USA). *Airframe*. Accessed: Mar. 5, 2022. [Online]. Available: levitatetech.com

[15] S. Iranzo, A. Piedrabuena, D. Iordanov, U. Martinez-Iranzo, and J.-M. Belda-Lois, "Ergonomics assessment of passive upper-limb exoskeletons in an automotive assembly plant," *Appl. Ergonom.*, vol. 87, Sep. 2020, Art. no. 103120.

[16] S. Kim, M. A. Nussbaum, M. I. M. Esfahani, M. M. Alemi, S. Alabdulkarim, and E. Rashedi, "Assessing the influence of a passive, upper extremity exoskeletal vest for tasks requiring arm elevation: Part I "expected" effects on discomfort, shoulder muscle activity, and work task performance," *Appl. Ergonom.*, vol. 70, pp. 315–322, Jul. 2018.

[17] (Comau, Turin, Italy). *MATE*. Accessed: Mar. 5, 2022. [Online]. Available: https://mate.comau.com/

[18] I. Pacifico *et al.*, "An experimental evaluation of the proto-MATE: A novel ergonomic upper-limb exoskeleton to reduce workers' physical strain," *IEEE Robot. Autom. Mag.*, vol. 27, no. 1, pp. 54–65, Mar. 2020.

[19] (Ottobock, Duderstadt, Germany). *PAEXO*. Accessed: Mar. 5, 2022. [Online]. Available: paexo.com

[20] P. Maurice *et al.*, "Objective and subjective effects of a passive exoskeleton on overhead work," *IEEE Trans. Neural Syst. Rehabil. Eng.*, vol. 28, no. 1, pp. 152–164, Jan. 2020.

[21] (SuitX, Emeryville, CA, USA). *ShoulderX*. Accessed: Mar. 5, 2022. [Online]. Available: suitx.com

[22] L. Van Engelhoven and H. Kazerooni, "Design and intended use of a passive actuation strategy for a shoulder supporting exoskeleton," in *Proc. Wearable Robot. Assoc. Conf. (WearRAcon)*, 2019, pp. 7–12.

[23] (Skel-Ex, Rotterdam, The Netherlands). *SkelEx*. Accessed: Mar. 5, 2022. [Online]. Available: skelex.com

[24] A. de Vries, M. Murphy, R. Könemann, I. Kingma, and M. de Looze, "The amount of support provided by a passive arm support exoskeleton in a range of elevated arm postures," *IISE Trans. Occup. Ergonom. Human Fact.*, vol. 7, nos. 3–4, pp. 311–321, 2019.

[25] M. Tschiersky, E. E. G. Hekman, D. M. Brouwer, and J. L. Herder, "Gravity balancing flexure springs for an assistive elbow orthosis," *IEEE Trans. Med. Robot. Bionics*, vol. 1, no. 3, pp. 177–188, Aug. 2019.

[26] Z. Cheng, S. Foong, D. Sun, and U. X. Tan, "Algorithm for design of compliant mechanisms for torsional applications," in *Proc. IEEE/ASME Int. Conf. Adv. Intell. Mechatronics*, 2014, pp. 628–633.

[27] Z. Cheng, S. Foong, D. Sun, and U. X. Tan, "Towards a multi-DOF passive balancing mechanism for upper limbs," in *Proc. IEEE 14th Int. Conf. Rehabil. Robot. (ICORR)*, 2015, pp. 508–513.

[28] G. Radaelli and J. L. Herder, "Isogeometric shape optimization for compliant mechanisms with prescribed load paths," in *Proc. ASME Int. Design Eng. Tech. Conf. Comput. Inf. Eng. Conf. (DETC)*, vol. 5, Aug. 2014, pp. 1–11.

[29] G. Radaelli and J. L. Herder, "A monolithic compliant large-range gravity balancer," *Mech. Mach. Theory*, vol. 102, pp. 55–67, Aug. 2016.

[30] G. Radaelli and J. L. Herder, "Shape optimization and sensitivity of compliant beams for prescribed load-displacement response," *Mech. Sci.*, vol. 7, no. 2, pp. 219–232, 2016.

[31] P. de Leva, "Adjustments to Zatsiorsky-Seluyanov's segment inertia parameters," *J. Biomech.*, vol. 29, no. 9, pp. 1223–1230, 1996.

[32] E. Rocon *et al.*, *Human–Robot Physical Interaction*. New York, NY, USA: Wiley, 2008, ch. 5, pp. 127–163.

[33] A. Oosterwijk, M. Nieuwenhuis, C. van der Schans, and L. Mouton, "Shoulder and elbow range of motion for the performance of activities of daily living: A systematic review," *Physiotherapy Theory Pract.*, vol. 34, no. 7, pp. 505–528, 2018.

[34] J. B. Jonker and J. P. Meijaard, "SPACAR—Computer program for dynamic analysis of flexible spatial mechanisms and manipulators," in *Multibody Systems Handbook*, W. Schiehlen, Ed. Berlin, Germany: Springer, 1990, pp. 123–143.

[35] J. P. Meijaard, "Fluid-conveying flexible pipes modeled by large-deflection finite elements in multibody systems," *J. Comput. Nonlinear Dyn.*, vol. 9, no. 1, 2014, Art. no. 11008.

[36] B. M. Friedrich, "Frenet_Robust.Zip." 2022. [Online]. Available: https://www.mathworks.com/matlabcentral/fileexchange/47885-frenet_robust-zip

[37] H.-S. Kim, J.-K. Min, and J.-B. Song, "Multiple-degree-of-freedom counterbalance robot arm based on slider-crank mechanism and bevel gear units," *IEEE Trans. Robot.*, vol. 32, no. 1,pp. 230–235, Feb. 2016.